# Polymer Chemistry



PAPER View Article Online
View Journal | View Issue



**Cite this:** *Polym. Chem.*, 2020, **11**, 4760

# Enhancing the toughness of composites *via* dynamic thiol—thioester exchange (TTE) at the resin—filler interface†

Nancy Sowan, <sup>1</sup>

<sup>a</sup> Yinan Lu, <sup>b</sup> Kevin J. Kolb, <sup>a</sup> Lewis M. Cox, <sup>c</sup> Rong Long <sup>b</sup> and Christopher N. Bowman <sup>1</sup>

<sup>b</sup>

\*a,d</sup>

Due to a mismatch in mechanical moduli, the interface between constituent materials in a composite is the primary locus for crack nucleation due to stress concentration. Relaxation of interfacial stresses, without modifying the properties of constituent materials, is a potent means of improving composite performance with broad appeal. Herein, we develop a new type of adaptive interface that utilizes thiol—thioester exchange (TTE) at the filler—polymer interface. Specifically, dynamic covalent bonds sequestered at material interfaces are reversibly exchanged in the presence of thioester moieties, excess thiol and a base/nucleophile catalyst. Employing this active interface effectively mitigates deleterious growth of interfacial stresses, thereby enhancing the composite's mechanical performance in terms of reductions in polymerization shrinkage stress and improvement in toughness. Activating interfacial TTE in an otherwise static matrix resulted in 45% reduction in the polymerization stress, more significant post-polymerization stress relaxation and drastically increased toughness relative to control composites incapable of TTE bond exchange but otherwise identical. In particular, the higher fracture toughness in TTE-activated composites is attributed to the alleviation of crack tip strain concentration, as revealed by digital image correlation.

Received 17th April 2020, Accepted 5th June 2020 DOI: 10.1039/d0py00563k

rsc.li/polymers

#### Introduction

Polymers reinforced with rigid fillers (*e.g.*, glass beads, silica and alumina particles) are widely used in many engineering fields due to the flexibility they provide in targeting desired physical and mechanical properties. Nanocomposites are of particular interest when designing composites of higher stiffness, due to the enormous surface area associated with nanofillers. <sup>1,2</sup> It is well known that the interfacial region in such polymers concentrates stresses due to the common mismatch in mechanical moduli between constituent materials, which negatively impacts the overall mechanical properties. <sup>3</sup> Accordingly, several decades of work have been directed towards reducing the interfacial stress, improving stress trans-

Recently, mechanoresponsive DCC-based composites, such as addition fragmentation chain transfer (AFT) based dental composites, <sup>6,7</sup> interfacial transesterification-based composites, <sup>8-10</sup> and disulfide-based vitrimer composites, <sup>11</sup> have been developed. A unique adaptive interface platform was introduced to effectively mitigate the interfacial stress and improve the overall mechanical properties by localizing AFT moieties only at the matrix–filler interface. However, composites with AFT-active filler are capable of undergoing stress relaxation at the interface only during light exposure which is

fer between fillers and the matrix, and examining impacts of filler size, content and the adhesive strength.<sup>2</sup> Despite these efforts, alleviating the concentration of interfacial stresses in order to prevent premature composite failure and improve crack-growth resistance is an ongoing challenge. Motivated by this limitation, recent developments in dynamic polymer composites have showcased the incorporation of dynamic covalent chemistries (DCCs). The presence of DCC-capable moieties in the resin formulation leads to chemical bond reshuffling and promotes stress relaxation while maintaining connectivity of the polymer network. These dynamic networks exhibit static thermoset properties under ordinary circumstances but reversibly rearrange covalent bonds, often in response to an externally applied stimulus.<sup>4,5</sup>

<sup>&</sup>lt;sup>a</sup>Materials Science and Engineering Program, University of Colorado, Boulder, CO 80309-0596. USA. E-mail: Christopher.Bowman@colorado.edu

<sup>&</sup>lt;sup>b</sup>Department of Mechanical Engineering, University of Colorado, Boulder, CO, 80309, USA

<sup>&</sup>lt;sup>c</sup>Mechanical and Industrial Engineering, Montana State University, Bozeman, MT 59717, USA

<sup>&</sup>lt;sup>d</sup>Department of Chemical and Biological Engineering, University of Colorado, Roulder, CO 80309-0596, USA

<sup>†</sup>Electronic supplementary information (ESI) available. See DOI: 10.1039/d0py00563k

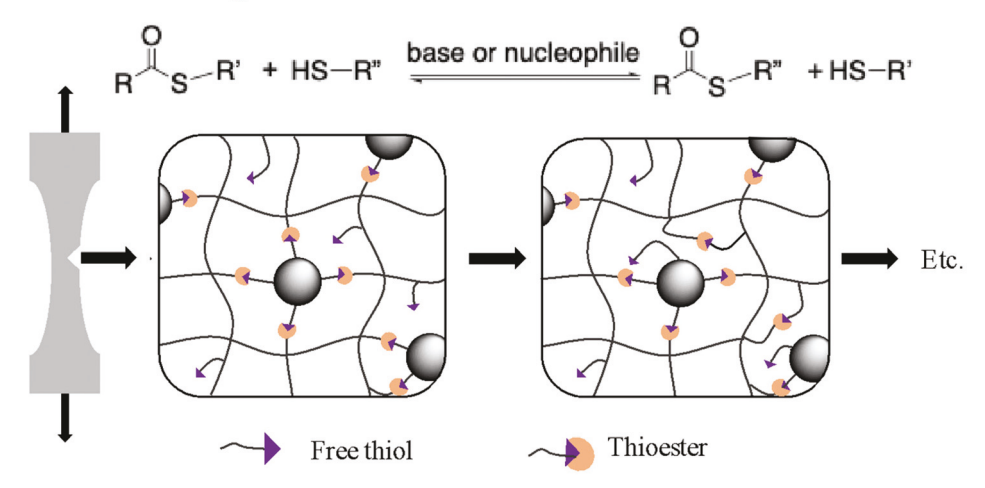
**Polymer Chemistry** Paper

required for generating short-lived radicals, thus offering minimal capacity for stress relaxation over the lifetime of the composite or in areas where light exposure is limited (e.g., optically thick).12

To address AFT's shortcomings, a perpetual, light independent interfacial DCC mechanism is examined here: the anionmediated thiol-Thioester Exchange (TTE) reaction. Exchange reactions involving thioesters have been effectively utilized to develop native chemical ligation (NCL),13 degradable hydrogel networks, 14 synthetic sequence-controlled polymers, 15 and to increase refractive indices in bulk polymers. 16 However, the dynamic behavior in such crosslinked networks was not explored until Worrell et al. published the first work introducing TTE reaction as a new class of covalent adaptable networks (CANs) that enables rapid, continuous ambient temperature stress relaxation.<sup>17</sup> This exchange reaction only proceeds under the condition that free thiol, thioester, and base/nucleophile as a catalyst are all present in the network. The nucleophile-promoted thiol-thioester exchange reaction happens when the nucleophilic catalysts attack the carbonyl of the thioester, forming a zwitterionic intermediate and a thiolate anion, followed by the regeneration of the nucleophilic catalyst and exchanging the thiol and thioester (Fig. 1A).18 If any of these three elements are missing, the polymer behaves as a typical crosslinked elastomer.17 This dynamic exchange reaction has been demonstrated in bulk materials, 17,19 and recently has been used to relax interfacial stresses in composite restorative materials.20

Therefore, following the successful demonstration by Worrell et al. indicating the efficiency of the TTE reactions<sup>17</sup> and the exceptional efficiency of interface-limited DCC processes in composites<sup>12,20</sup> herein silica nanoparticles (SNP) were functionalized using a silane that contains a TTE moiety capable of bond exchange and subsequently dispersed into a thiol-ene resin. By localizing TTE to the resin filler interface, adaptive interfaces capable of stress relaxation and dynamic bond exchange were created (Fig. 1A). As previously demonstrated; composites where DCC is limited to the interface exhibit comparable enhancement of mechanical properties to the composite where DCC occurs only in the resin, without

#### A) Thiol-Thioester Exchange:



#### B) Resin Formulation:

Fig. 1 (A) Mechanism and illustration for TTE at the SNP-polymer interface. (B) Monomers and fillers used in the formulation of the composites. Resins were formulated of PETMP and TATATO (1.1:1 SH:ene), 2 wt% DABCO and 10 wt% of SNPs, either TTE or the corresponding control. Polymerization was initiated with 1 wt% of I819 (bis(2,4,6-trimethylbenzoyl)-phenylphosphineoxide) visible light photoinitiator, and photocured with 400-500 nm visible light at 50 mW cm<sup>-2</sup> for 5 min on each side and then postcured in an oven at 60 °C for 4 h.

**Paper Polymer Chemistry** 

altering the resin's formulation. 12,20 This behavior manifests as enhanced stress relaxation and improved mechanical performance. Due to the long catalytic lifetime of the base/nucleophile catalysts, such systems undergo continuous exchange of covalent bonds that spans the interface and continues to relax the interfacial stress over the lifetime of the composite - not just during or shortly after the polymerization. Strikingly, in situ interfacial bond exchange is observed to directly impact and even fundamentally change the fracture processes, delaying crack propagation and displaying unique failure mechanisms in these TTE-activated dynamic composites.

# Results

To develop a TTE-based adaptive interface and examine its influence on composite behavior, SNPs were functionalized using a silane that had a thioester moiety capable of bond exchange and dispersed with 10 wt% particle loading into photopolymerizable thiol-ene resin, as illustrated in Fig. 1. The static resin was comprised of a triene monomer (1,3,5triallyl-1,3,5-triazine-2,4,6(1H,3H,5H)-trione (TATATO)) and a tetrathiol(pentaerythritol tetra(3-mercaptopropionate (PETMP)) with 10% excess thiol and 2 wt% 1,4-diazabicyclo [2.2.2]octane (DABCO) nucleophile (Fig. 1B). An identical control sample, unable to undergo TTE bond exchange through the elimination of the TTE moiety from the interface or the catalyst necessary for the bond exchange, was also formulated. The thiolated control illustrated in Fig. 1 was used in the following experiments unless otherwise stated. The control composite exhibited a similar  $T_{\rm g}$  and storage modulus at ambient conditions ( $T_{\rm g} \approx 60$  °C, Fig. S1†), which allows us to decouple the effects caused by the interfacial bond-exchange process. It should be noted that both the control- and TTEbased composites showed very similar dispersion of the SNPs using SEM imaging (Fig. S2†).

Residual stress is known to arise during polymerization, due to post-gelation volumetric contraction and elastic modulus development primarily during vitrification, leading reduced mechanical performance and premature failure. 21,22 The design of mechanically robust glassy networks with low polymerization-induced shrinkage stress at quantitative conversion is particularly desired in the application of bulk materials. To investigate the effect of interfacial TTE bond exchange on shrinkage stress reduction within a composite system, the real-time polymerization kinetics, and the corresponding stress generated due to the shrinkage on both control and TTE-activated composites were monitored via an FTIR spectrometer connected to a tensometer. Fig. 2A shows the evolution of shrinkage stress of the TTE composite as compared to the shrinkage stress developed in the control at equivalent conversion. A significant (45%) reduction in the polymerization shrinkage stress was achieved in the composites with activated TTE at the particles interface as compared with the TTE-free composites used in the control experiment at equivalent 90% conversion (Fig. 2A). While interfacial relaxation should intuitively be capable of reducing shrinkage stress, the dramatic improvement here is enabled by the high surface area to volume ratio of SNPs.

To assess the influence of TTE bond exchange in fully cured, glassy composites ( $T_g = 60$  °C as measured in DMA) and examine the ability of interfacial TTE bond exchange to relieve stress during mechanical loading, stress relaxation experiments were conducted by applying a constant 1% tensile strain to both TTE-based and control composites at ambient temperature. Composites with activated TTE at the particle interface exhibited a significant 50% stress relaxation within 30 minutes even though the bulk resin is not capable of any DCC. In contrast, the control composites showed minimal stress relaxation, typical of glassy thermosets (Fig. 2B). This ability to relax stresses is a key demonstration of how interfacial dynamic bond exchange can enhance composite performance under mechanical loading.

The highly repeatable stress relaxation during and after in situ polymerization of thiol-ene composites suggests that there are minimal limitations associated with side reactions such as for example disulfide formation. Any oxidation of thiols would be expected to increase the crosslinking, reduce the overall thiol content and consequentially affect, and likely diminish, the dynamic response. Stable dynamic response is suggestive of the insignificant impact of these undesired side reactions that might otherwise consume the thiol functional

To examine the influence of interfacial bond exchange on the strength and toughness of glassy composites under mechanical loading, tensile testing was conducted with a constant strain rate of 0.006 min<sup>-1</sup> until failure. Such a low strain rate was selected to enable sufficient time for stress relaxation to occur via the bond exchange prior to failure. Since the mechanical properties are highly dependent on the strain rate, 23-25 this material shows extended plastic deformation, with a relatively low tensile modulus. Composites with activated TTE at the interface exhibited significantly higher tensile strength and 3-4 times greater toughness than the control composite (Fig. 2C & Table S1†). Interestingly, in addition to the dramatic increase in toughness, different failure modes were also observed in the control and TTE-activated samples. The control samples showed a typical brittle failure mode for a glassy composite, where at the peak stress, a crack appeared and catastrophically propagated across the sample, providing no early indication of upcoming failure. However, a different failure mode was observed in the TTE-activated samples, where an initial crack formed and then propagated across the sample as would normally be observed in the control, but the crack propagation was eventually arrested, and the stress plateaued. Subsequent increases in stress nucleated a second crack on the opposite side of the sample. The two cracks then merged and the sample failed catastrophically (Fig. 2C). This shift in fracture behavior along with the corresponding increase in the toughness relative to control samples are related to the ongoing interfacial stress relaxation during tensile loading. During tensile tests, the energetic barrier to

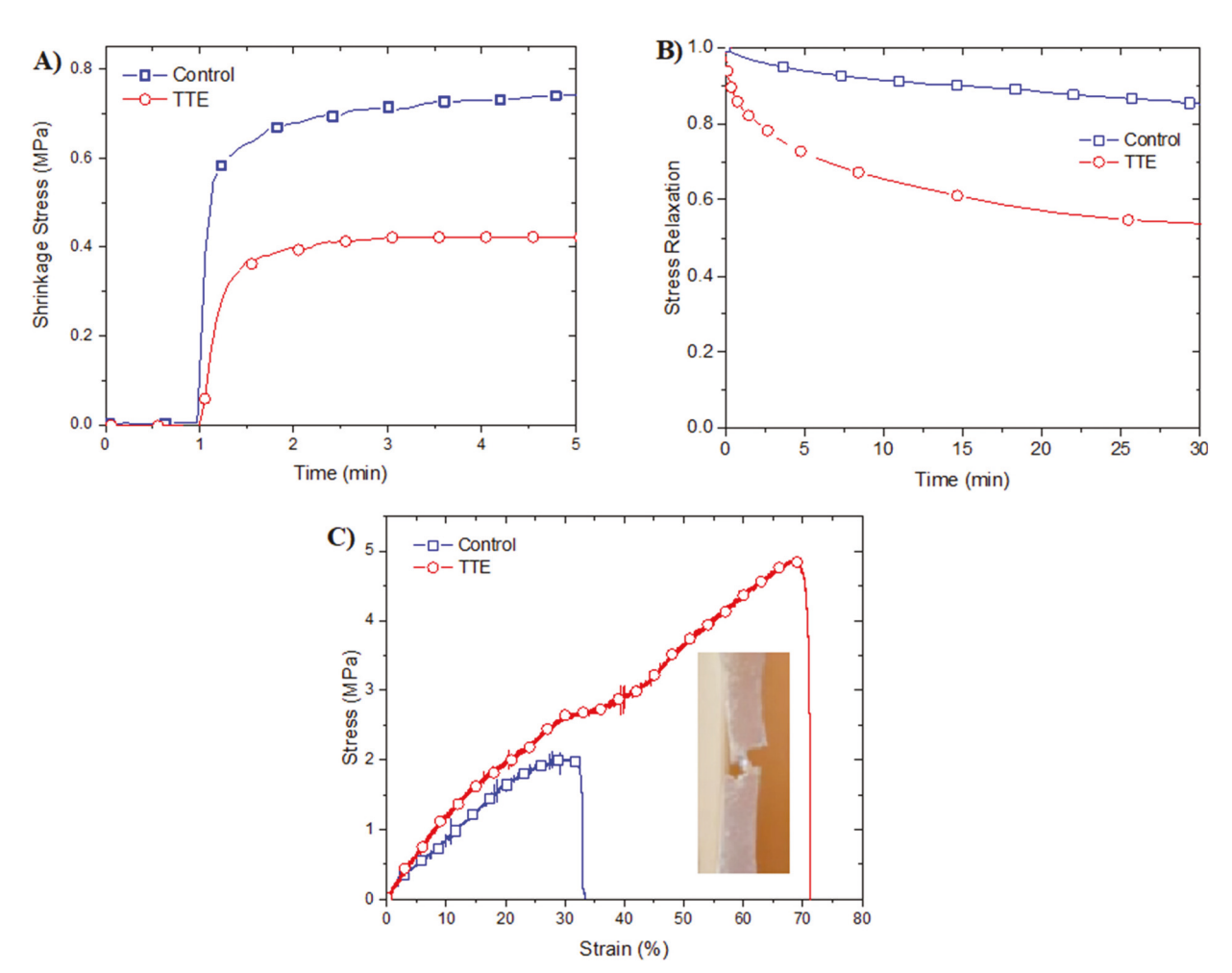


Fig. 2 (A) In situ polymerization stress of both control (squares) and TTE (circles) composites. Samples were placed between two quartz rods, previously treated with a thiol-functional silane and irradiated for 5 min at ambient temperature with 400–500 nm light at 50 mW cm<sup>-2</sup> following 1 min in the dark to establish a baseline measurement. (B) Stress relaxation achieved in fully cured 0.25 mm thick sample of control (squares) and TTE (circles) composite at constant 1% strain. (C) Tensile test for fully cured, dogbone-shaped samples of both control and TTE-activated composites at a strain rate of 0.006 min<sup>-1</sup>. The inset shows the image of a TTE-activated composite sample after failure.

chain scission in the polymer resin reduces, generating defects and leading to failure.<sup>26,27</sup> Having exchangeable bonds at the particle interface in TTE composite acts to counter this effect by relaxing chain conformation, reducing the stress at the crack tip that drives the crack propagation, and hence delaying failure.

Motivated by the different failure mechanisms observed in tensile experiments, notched samples of control and TTE-activated composites (Fig. 3A) were used to study how TTE affects the deformation of a pre-existing crack before it starts to propagate. Initially, both the notched control and TTE-activated samples were subjected to continuous tensile loading at the same global strain rate (0.025 min<sup>-1</sup>). It was observed that the crack in the control sample started to propagate when the global strain  $\Delta/h$  achieved 3%. Therefore, for the control sample the global strain was held fixed at 3% for 5 minutes to stabilize crack propagation (see Fig. 3A), during which time the crack tip advanced ~0.6 mm. After that period, the control sample was again subjected to continuous loading until frac-

ture was complete. For the TTE-activated sample, the global strain was also held fixed at 3% to facilitate comparison with the control sample. After 3 minutes of fixed global strain, the crack remained stationary in the TTE-activated sample, and therefore, it was again subjected to continuous loading until fracture was complete. Crack propagation in the TTE-activated sample did not occur until the global strain reached 6.7%. As shown in Fig. 3B, initially the notched control and TTE-activated samples exhibited similar compliance, but the TTE-activated sample was able to sustain a higher peak force than the control. Digital Image Correlation (DIC) was used to map the strain fields in both notched samples (Video S1†). Results of the normal strain component  $\varepsilon_{yy}$  along the tensile direction, shown in Fig. 3C, revealed a striking difference. In the control sample, a significant concentration of  $\varepsilon_{yy}$  near the crack tip emerged as the external loading increased, which manifests severely amplified stress at the crack tip. The crack tip stress concentration causes localized material failure and hence crack propagation.<sup>28</sup> In contrast, the  $\varepsilon_{yy}$  field in the TTE Paper

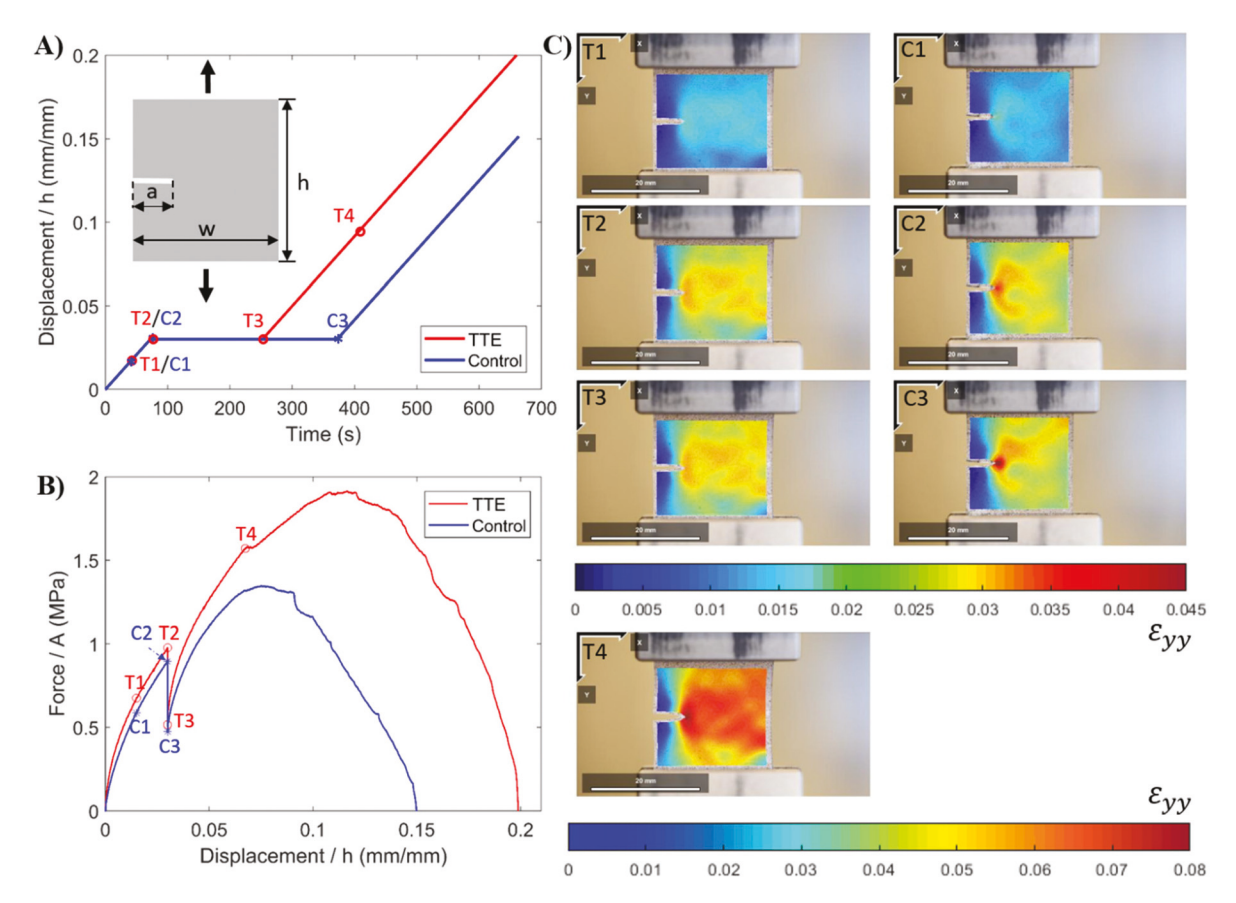


Fig. 3 (A) Loading history in terms of the global strain Δ/h versus time and (B) nominal tensile stress (force/cross-section area) versus global strain of the single edge notch fracture test using the control and TTE-activated samples. (C) Spatial distribution of the vertical normal strain component  $\varepsilon_{yy}$ , measured using DIC, at different time frames before crack propagation: T1/C1 (global strain = 1.5%, no crack propagation); T2/C2 (global strain = 3%, crack propagation started in C2); T3/C3 (global strain = 3%, crack propagation continued in C3); T4 (global strain = 6.7%, crack propagation started).

sample was more diffusive, as reflected in the lower strain at the crack tip but higher strain far ahead of the crack tip as compared to the control sample. This result suggests that the TTE process was able to alleviate crack tip strain concentration through stress relaxation, which led to crack tip blunting and delocalized material failure, reminiscent of the toughening effects of plasticity in metals.29 The DIC experiment was repeated for other TTE and control samples under continuous loading, where similar observations regarding the crack tip strain concentration were found (Fig. S3†).

To quantify the toughening effect of TTE, the Griffith fracture criterion were applied to the notched samples, i.e., whether a crack can propagate or not is governed by a competition between the energy release rate G and the fracture energy  $\Gamma$  (unit: J m<sup>-2</sup>).<sup>29</sup> The former, G, is the energy available to drive crack propagation per unit area and represents structural effects such as the external loading and sample geometry. The latter,  $\Gamma$ , defined as the energy required to advance the crack by a unit area, describing the material's resistance to fracture. Initiation of crack propagation occurs when G exceeds  $\Gamma$ . The critical value  $G_c$  at the onset of crack propagation is taken as the fracture energy  $\Gamma$ . As shown in Fig. S4A,†

both the control and TTE composites can be approximated as linear elastic materials with about the same modulus before unloading occurs. The theory of linear elastic fracture mechanics predicts that the crack opening should follow a parabolic profile (Fig. S4B†), the amplitude of which is related to the energy release rate  $G^{29}$ . By fitting the crack opening shape at the onset of crack propagation with the parabolic profile (Fig. S4C and D†),  $G_c$  for the TTE sample in Fig. 3 was found to be 550 J m $^{-2}$ , over twice that of  $G_c$  for the control sample  $(260 \text{ J m}^{-2}).$ 

The notched sample tests in Fig. 3 focus on the crack deformation before propagation. To highlight further the effect of the TTE adaptive interfaces on the crack propagation behavior, three-point bending tests were performed on a twonotch sample where one notch is double the length of the other, with a crosshead speed of 0.75 mm min<sup>-1</sup> until fracture (Fig. 4A). The dimensions of each specimen used in the investigation were  $2 \times 4 \times 20 \text{ mm}^3$  with 3 mm and 1.5 mm cracks on one edge. The control composite failed in a brittle manner, with propagation of the longer crack happening at 1 mm displacement as shown in Fig. 4A-1 & Video S2.† In contrast, by activating the TTE at the resin/filler interface, the

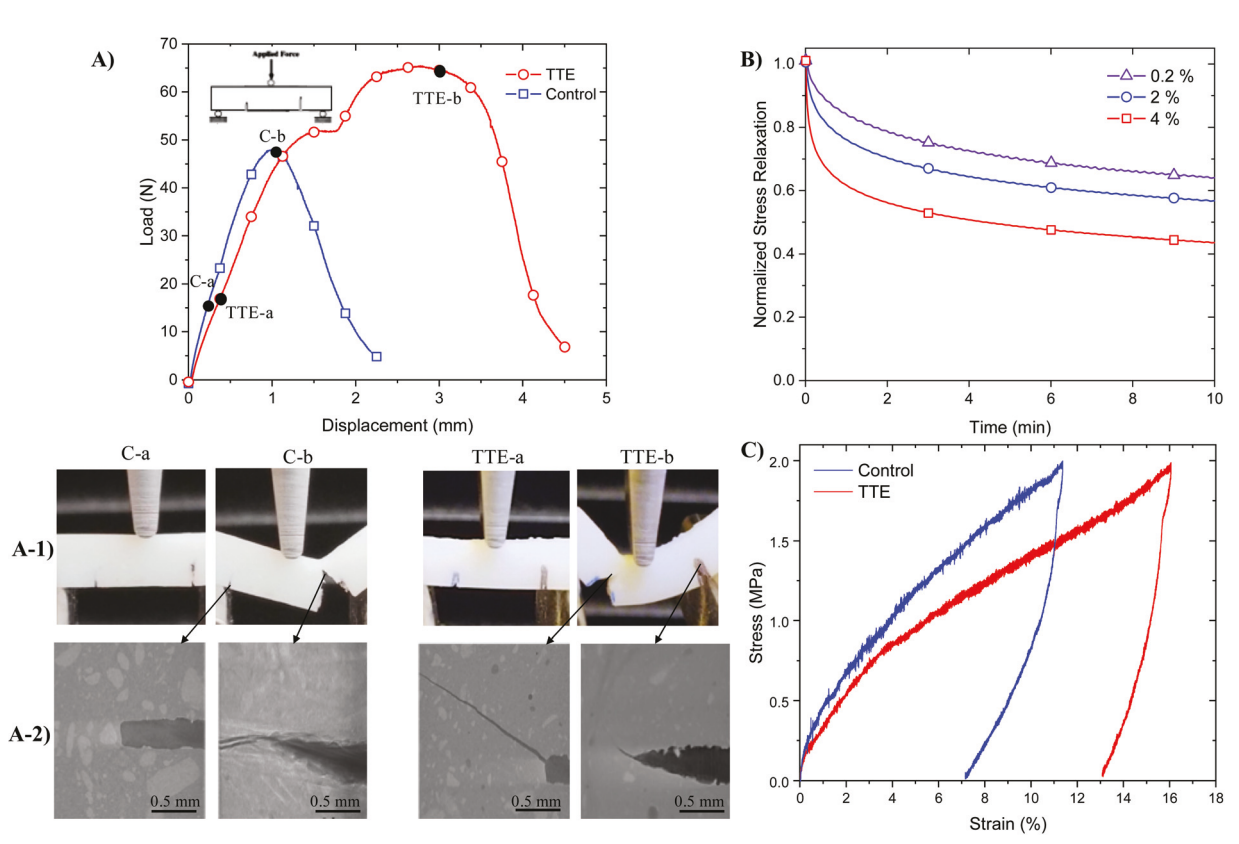


Fig. 4 (A) Load—displacement profiles from fracture of double-notched composite specimens for: Control composites (blue square) and dynamic TTE-activated composites (red circle) at a displacement rate 0.75 mm min<sup>-1</sup>. (A-1) Images of the two uneven notches before and after failure. The non-dynamic control, as with other conventional materials, fails at the large notch whereas the TTE-activated material initially yields at the large notch up to approximately 15% strain after which the small notch grows and is the locus of failure. (A-2) Micro X-ray Computed Tomography (MXCT) images of fractured surfaces of the two cracks for both control and TTE-enabled composites. (B) Stress relaxation of TTE composite at different strain (0.2% (purple triangle), 2% (blue circle) and 4% (red square)). (C) First hysteresis loop cycle during loading of 2 MPa stress then unloading to 0 MPa at 0.006 min<sup>-1</sup> rate for both control and TTE-activated composite.

failure process became more ductile. Fig. 4A-1 & Video S3† show that in TTE-activated samples the initial crack propagation also began at the tip of the longer crack, but the propagation was slow compared to the control and was eventually arrested. As the displacement loading continued to increase, the shorter crack began to propagate and ultimately caused failure. The arrest of the longer crack resulted in  $\approx 3$  times the total energy (6.1  $\pm$  0.9 (MJ m<sup>-3</sup>)) being absorbed before material failure when compared to the control (1.9  $\pm$  0.5 (MJ m<sup>-3</sup>)) (Table S2†). A second control sample identical to the TTE-sample but unable to undergo TTE bond exchange due to the elimination of the DABCO catalyst, was also tested and confirmed our conclusion by failing in a conventional manner (Fig. S5†).

The morphology of fractured surfaces was characterized by utilizing a Micro X-ray Computed Tomography (MXCT, ZEISS Xradia 520 Versa) to capture post-mortem images of the cracks in control and TTE composites. As shown in Fig. 4A-2, the control sample failed by continuous crack growth at the initially longer crack, before the shorter crack even started to grow, while fractured surfaces of TTE indicate that the initially longer crack propagated for only  $\approx\!100~\mu m$  then stopped

growing and the shorter one catastrophically propagated to cause the ultimate failure (Fig. 4A-2).

The difference in crack propagation behavior in the TTE and control samples is interpreted by considering how the energetic driving force G and resistance  $\Gamma$  change as the crack propagates. The change in G is governed by structural effects such as external loading conditions, sample geometry and crack length. On the other hand,  $\Gamma$  typically increases upon crack propagation in materials with hysteretic behavior due to the expansion of a dissipation zone around the crack tip, known as crack growth resistance.29 For the control composite, the concentrated crack tip strain field and the brittle fracture mode imply that the increase in  $\Gamma$  upon crack propagation should be insignificant. Therefore, the fact that the longer crack in the control sample propagated catastrophically suggests that G should increase with crack length, i.e., structurally the test geometry in Fig. 4A favors continuous growth of the longer crack. Since the TTE and control samples are subjected to the same geometry and loading condition, structural effects should also favor continuous growth of the longer crack in the TTE sample. However, the longer crack in the TTE composite was arrested, implying that  $\Gamma$  must also increase with

crack length. This phenomenon, attributed to the TTE-induced stress relaxation and energy dissipation at the crack tip,  $^{30,31}$  can stabilize the propagation of the longer crack if it surpasses the structural effects for G that favor continuous growth.

Another peculiar observation in the TTE sample is that the shorter crack took over the propagation after the longer crack was arrested. Fig. 4A-2 reveals that the shorter crack propagated at an angle with the original direction, indicating an interplay between Mode-I (tensile) and Mode-II (in-plane shear) in the local stress field.<sup>29</sup> A detailed analysis on the propagation of the shorter crack would require knowledge regarding the mixed-mode dependence of the fracture energy  $\Gamma$  and is not pursued here. Instead, the fact that the short crack was able to propagate indicates that the stress field around its tip did not experience significant relaxation by the TTE reaction during the propagation of the long crack. Based on this argument, we hypothesize that higher stress leads to faster TTE-induced relaxation by increasing the reaction kinetics. Initially the higher stress at the longer crack accelerates the relaxation which eventually leads to its arrest. During this process, the shorter crack did not experience the same extent of stress relaxation, which allowed it to propagate after the arrest of the long crack. To verify this hypothesis, the time history of stress relaxation at three different fixed strain levels was measured (Fig. 4B). Accelerated relaxation rate was noticed by increasing the strain levels from 0.2% to 2% to 4%. At 0.2% strain 35% stress relaxation was achieved in 10 minutes, while the same degree of relaxation was achieved in 30 s at 4% strain, which clearly support our hypothesis. In addition, cyclic loading at three different stress levels, 0.5 MPa, 2 MPa and 4 MPa up to 3 loading-unloading cycles was performed. The ratio between the dissipative energy and the released energy was calculated at the three stress levels and is presented in Fig. S6.† Higher stress levels systematically resulted in higher ratios of dissipative energy to the released energy, due to the accelerated, more efficient bond exchange, congruent with Fig. 3B.

To investigate how TTE bond exchange affects the polymer composites at long time scales, a cyclic loading to 2 MPa stress was applied on both TTE and control composites, followed by unloading and reloading of the stress until the composite's failure. The hysteresis curves are presented in Fig. 4C & Fig. S7.† Upon load release, TTE-based composites systematically exhibit a greater degree of both energy dissipation and non-recoverable strain when compared to the control. Additionally, the TTE composite was found to survive more than 20 cycles without observable crack nucleation while the control composites without any interfacial DCC were only able to survive 3-4 such cycles as illustrated in Fig. S7.† The cyclic loading tests, interpreted as an accelerated fatigue experiment, suggest that the resin/filler interfacial relaxation leads to longer composite lifetime when under mechanical loading. Applications such as vibration dampeners, shock absorbers, protective coatings, dental materials, and others would benefit from the enhanced mechanical performance and the resistance to failure that result from a reduction in interfacial stress.

# Conclusion

The efficiency of TTE bond exchange as a new light independent, interfacial DCC mechanism that can undergo continuous bond reshuffling through the lifetime of polymer composites was examined here. As evidenced above, this platform significantly improves the composite's mechanical performance by relaxing the interfacial stress, despite the presence of TTE only at the interface with very low concentration. Activating TTE bond exchange at the polymer-particle interface enables the composites to significantly increase the degree of interfacial stress relaxation, resulting in 45% reduction in polymerization stress, 50% stress relaxation when fully cured, glassy composite is under mechanical loading, 3-4 times improvement in the toughness, and a fundamental shifting of the failure mechanism. Achieving this behavior represents a transformative technology to continuously relax the stress concentration at the polymer-filler interface with broad potential for applications in materials with different constituents, especially in opaque composites or when composites are under mechanical loading.

# Conflicts of interest

There are no conflicts to declare.

# Acknowledgements

The authors acknowledge financial support from the National Science Foundation (NSF CHE 13012296). Y. L. and R. L. acknowledge the support from a National Science Foundation CAREER award (NSF CMMI-1752449). Additional thanks to Shane Fraizer for assistance in performing Micro X-ray Computed Tomography experiment (MXCT).

#### References

- 1 Q. Chen, I. Chasiotis, C. Chen and A. Roy, *Compos. Sci. Technol.*, 2008, **68**, 3137–3144.
- 2 S. Y. Fu, X. Q. Feng, B. Lauke and Y. W. Mai, *Composites, Part B*, 2008, **39**, 933–961.
- 3 D. Eiras and L. A. Pessan, Mater. Res., 2009, 12, 517-522.
- 4 C. J. Kloxin and C. N. Bowman, Chem. Soc. Rev., 2013, 42, 7161–7173.
- 5 C. J. Kloxin, T. F. Scott, B. J. Adzima and C. N. Bowman, *Macromolecules*, 2010, 43, 2643–2653.
- 6 H. Y. Park, C. J. Kloxin, A. S. Abuelyaman, J. D. Oxman and C. N. Bowman, *Macromolecules*, 2012, 45, 5640–5646.
- 7 H. Y. Park, C. J. Kloxin, M. F. Fordney and C. N. Bowman, *Macromolecules*, 2012, 45, 5647–5652.

Polymer Chemistry Paper

- 8 M. Qiu, S. Wu, Z. Tang and B. Guo, Compos. Sci. Technol., 2018, 165, 24–30.
- 9 A. Legrand and C. Soulié-Ziakovic, *Macromolecules*, 2016, 49, 5893–5902.
- 10 Z. Tang, Y. Liu, B. Guo and L. Zhang, *Macromolecules*, 2017, **50**, 7584–7592.
- 11 A. R. de Luzuriaga, R. Martin, N. Markaide, A. Rekondo, G. Cabañero, J. Rodríguez and I. Odriozola, *Mater. Horiz.*, 2016, 3, 241–247.
- 12 N. Sowan, L. M. Cox, P. K. Shah, H. B. Song, J. W. Stansbury and C. N. Bowman, *Adv. Mater. Interfaces*, 2018, 5, 1800511.
- 13 B. L. Nilsson, N. B. Soellner and R. T. Raines, Annu. Rev. Biophys. Biomol. Struct., 2005, 34, 91–118.
- 14 C. Ghobril, K. Charoen, E. K. Rodriguez, A. Nazarian and M. W. Grinstaff, *Angew. Chem., Int. Ed.*, 2013, **52**, 14070–14074.
- 15 J. L. Price, E. B. Hadley, J. D. Steinkruger and S. H. Gellman, *Angew. Chem.*, *Int. Ed.*, 2010, **49**, 368–371.
- 16 J. Liu and M. Ueda, J. Mater. Chem., 2009, 19, 8907.
- B. T. Worrell, M. K. McBride, G. B. Lyon, L. M. Cox,
   C. Wang, S. Mavila, C.-H. Lim, H. M. Coley,
   C. B. Musgrave, Y. Ding and C. N. Bowman, *Nat. Commun.*, 2018, 9, 2804.
- 18 B. T. Worrell, S. Mavila, C. Wang, T. M. Kontour, C. H. Lim, M. K. McBride, C. B. Musgrave, R. Shoemaker and C. N. Bowman, *Polym. Chem.*, 2018, 9, 4523–4534.

- 19 C. Wang, S. Mavila, B. T. Worrell, W. Xi, T. M. Goldman and C. N. Bowman, ACS Macro Lett., 2018, 7, 1312–1316.
- 20 N. Sowan, A. Dobson, M. Podgorski and C. N. Bowman, *Dent. Mater.*, 2020, **36**, 53–59.
- 21 L. F. J. Schneider, L. M. Cavalcante and N. Silikas, *J. Dent. Biomech.*, 2010, **1**, 131630–131630.
- 22 H. B. Song, N. Sowan, P. K. Shah, A. Baranek, A. Flores, J. W. Stansbury and C. N. Bowman, *Dent. Mater.*, 2016, 32, 1332–1342.
- 23 E. Kontou and A. Kallimanis, *Compos. Sci. Technol.*, 2006, 66, 1588–1596.
- 24 S. V. Thiruppukuzhi and C. T. Sun, Compos. Sci. Technol., 2001, 61, 1–12.
- 25 R. Fracasso, M. Rink, A. Pavan and R. Frassine, *Compos. Sci. Technol.*, 2001, **61**, 57-63.
- 26 J. a. Odell, a. Keller and Y. Rabin, J. Chem. Phys., 1988, 88, 4022–4028.
- 27 G. H. Michler and H.-H. K.-B. von Schmeling, *Polymer*, 2013, 54, 3131–3144.
- 28 P. Adriaensens, L. Storme, R. Carleer, D. Vanderzande, J. Gelan, V. M. Litvinov and R. Marissenf, *Macromolecules*, 2000, 33, 4836-4841.
- 29 A. T. Zehnder, Fracture Mechanics, Springer, US, 2012.
- 30 Y. Qi, J. Caillard and R. Long, *J. Mech. Phys. Solids*, 2018, **118**, 341–364.
- 31 T. Zhang, S. Lin, H. Yuk and X. Zhao, *Extrem. Mech. Lett.*, 2015, 4, 1–8.

Electronic Supplementary Material (ESI) for Polymer Chemistry. This journal is © The Royal Society of Chemistry 2020

# **Supporting Information**

# **Enhancing the Toughness of Composites via Dynamic Thiol-Thioester Exchange (TTE) at**the Resin-Filler Interface

Nancy Sowan<sup>a</sup>, Yinan Lu<sup>b</sup>, Kevin J. Kolb<sup>a</sup>, Lewis M. Cox<sup>c</sup>, Rong Long<sup>b</sup>, and Christopher N.

#### Bowman\*a,d

- <sup>a</sup> Materials Science and Engineering Program, University of Colorado, Boulder, CO 80309-0596, USA.
- <sup>b</sup> Department of Mechanical Engineering, University of Colorado, Boulder, CO, 80309, USA.
- <sup>c</sup> Mechanical and Industrial Engineering, Montana State University, Bozeman, MT 59717, USA.
- <sup>d</sup> Department of Chemical and Biological Engineering, University of Colorado, Boulder, CO 80309-0596, USA.

#### Materials and Methods.

Materials

tetrakis(3-mercaptopropionate) (PETMP), Triallyl-1,3,5-triazine-2,4,6-Pentaerytritol (1H,3H,5H)-trione (TATATO), 1,4-diazabicyclo[2.2.2]octane (DABCO), and propylamine were purchased from Sigma-Aldrich. Irgacure 819 (bis(2,4,6-trimethylbenzoyl)phenylphosphineoxide) was obtained from BASF. Schott glass (mean particle size 40 nm) untreated were generously donated by Evonik Silicas and used as the inorganic fillers. Prior to implementation and as described later, these fillers were subsequently functionalized with thiol group for inclusion and copolymerization in the composite. All chemicals were used as received. The thioester-diacrylate<sup>18</sup> was synthesized using methods reported elsewhere.

#### Filler Functionalization

4 g of silica particles (Schott, OX50, 40 nm) were first taken in a glass tube and heated at 165 °C under vacuum using a Buchi heater/condenser for 3 h. The dried nanoparticles were then transferred to a 250 mL bottom rounded flask containing 200 mL of anhydrous toluene

supplemented with 2 g of (3-Mercaptopropyl) trimethoxysilane prereacted for 10 min with 2 g of n-propylamine. The reaction mixture was then refluxed at 120 °C for 24 h. After silanization of nanoparticle, the liquid suspension was centrifuged and the solid pellets were collected thoroughly, and washed with toluene ( $3 \times \approx 25$  mL) and methylene chloride ( $3 \times \approx 25$  mL) in two separate washing/centrifugation cycles. The washed filler particles were dried under vacuum overnight at 70 °C. Then 2 g of the dried thiol functionalized fillers were reacted with 0.7 g thioester diacrylate in DCM in presence of 3 mL TEA base at R.T overnight. After reaction completion, these nanoparticles were washed with DCM ( $1 \times \approx 25$  mL), toluene ( $2 \times \approx 25$  mL) and DMSO ( $2 \times \approx 25$  mL), and dried under vacuum overnight at 70 °C. The functionalized particles were analyzed by DRIFT FT-IR spectroscopy and TGA. The mass loss difference between silanized and unfunctionalized fillers suggests successful functional group grafting on the surface of glass particles in each case. Also, the DRIFT FT-IR characterization provides evidence of silanol group disappearance around 3745 cm<sup>-1</sup> and the appearance of the thioester group around 1700 cm<sup>-1</sup>, implying successful surface modification.

#### Sample preparation

Mixtures of PETMP, TATATO (1.1:1 molar ratio of thiol:ene), with 1 wt% of I819 as visible light photoinitiator, 2 wt% of DABCO and 10 wt% of SNPs with either the TTE-functionalized adaptive interface or the corresponding control, were prepared. Silanized fillers and resins were blended in a speedmixer (DAC 150 FVZ, Flakteck) to ensure homogenous formulations. Samples were photocured with 400-500 nm visible light at 50 mW/cm² for 5 min on each side and then post-cured in an oven at 60 °C for 4 h.

## Fourier Transform Infrared Spectroscopy

An FT-IR spectrometer (Nicolet 6700) connected to a tensometer via fiber optic cables was used to monitor the real-time polymerization kinetics in concert with stress measurements. Samples were placed between two cylindrical quartz rods, and 300 mW cm<sup>-2</sup> light was irradiated from the bottom rod using a light guide connected to a mercury lamp (Acticure 4000, EXFO) with 400–500 nm bandgap filter. The overtone signal of double bonds between 6250–6096 cm<sup>-1</sup> was monitored during the FT-IR measurements.

# Polymerization Shrinkage Stress Measurement

Shrinkage stress was measured via a tensometer using cantilever beam deflection theory (American Dental Association Health Foundation, ADAHF–PRC). A composite paste (1 mm in thickness, 6 mm in diameter) was placed between two cylindrical quartz rods, which were previously treated with a methacrylate functional silane to promote bonding at the glass surface/resin interface. A 300 mW cm<sup>-2</sup> of light was irradiated from the bottom rod using a light guide connected to a mercury lamp (Acticure 4000, EXFO) with a 400–500 nm bandgap filter. Polymerization-induced shrinkage of sample exerted a tensile force which caused the deflection of the aluminum beam. A linear variable differential transformer was used to convert the displacement to shrinkage stress based upon beam calibration constant and cross-sectional area of the sample. For the simultaneous measurement of conversion with shrinkage stress, data were collected continuously for 10 min (n = 3).

## Thermogravimetric Analysis

TGA (Pyris 1, PerkinElmer) was used to analyze the functionalized silica nanoparticles. Each sample was run in a nitrogen atmosphere (20 mL min<sup>-1</sup>) from 50 to 850 °C at a heating rate of 10 °C min<sup>-1</sup>.

#### Fracture Test

The single edge notch geometry as shown in **Figure 3A** was adopted for the fracture test. The samples were in the form of rectangular thin sheets with width w = 22mm, height h = 20mm and thickness t = 0.4 mm. An initial crack with length a = 5mm was introduced at the edge of the sample by a razor blade. In order to measure the strain field using Digital Image Correlation (DIC), a speckle pattern was applied to the surface of the sample using paint spray (see sample image in **Figure S3** for example). After that the sample was mounted on a mechanical test machine (Intron 5965) for fracture test. The bottom boundary of the sample was fixed, while the top boundary was subjected to a vertical displacement  $\Delta$ . Although the strain field in the sample is locally non-uniform near the crack, the ratio  $\Delta/h$ , referred to as the global tensile strain, was used to quantify the loading. The displacement  $\Delta$  was applied at a constant rate of  $\Delta = 0.5$  mm/min which corresponds to a global strain rate of  $\Delta/h = 0.025$  min<sup>-1</sup>. During the test, a video of the sample deformation was recorded using a CCD camera (Canon EOS 6D DSLR along with Canon 100mm F/2.8L Macro Lens).

# Digital Image Correlation

Images of the fracture sample during loading were processed by a DIC software NCORR,<sup>19</sup> an open source code written in MATLAB (Mathworks, Natick MA). This software is capable of determining the displacement and strain fields by analyzing the speckle pattern on the sample

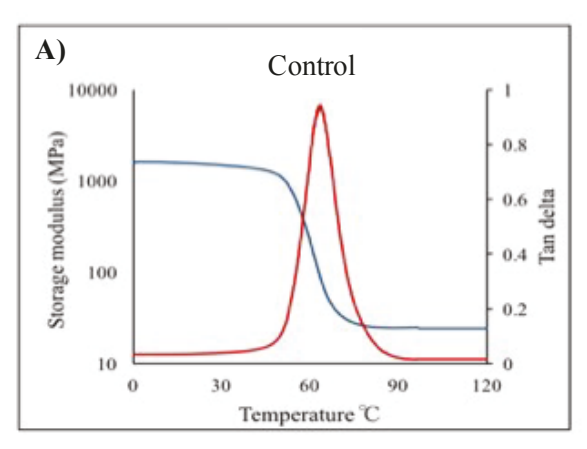
between the reference image and the deformed image.<sup>20</sup> The reference image was extracted from the initial frame of the video before the displacement loading was applied. The deformed image was extracted from the frames after the displacement loading was applied, and corresponded to a certain global strain  $\Delta/h$ . Three parameters, i.e., subset radius, subset spacing and strain radius, are required by NCORR to perform DIC, which were set to be 43 pixels, 3 pixels and 10 pixels, respectively, following the documentation of NCORR (http://www.ncorr.com/). Note that the images consisted of 1920×1080 pixels and the size of each pixel was 31.2  $\mu$ m. Through this process, we were able to obtain the displacement and strain fields for the fracture test as shown in Figure 3 and Video S1.

# Three-Point-Bending Test

Rectangular bars (2×4×20 mm) and 2 uneven notches (3-mm long notch and 1.5 mm short notch) on one edge were used for three-point bending tests to characterize the fracture behavior. The three-point bending tests were performed using a (MTS 858 Mini Bionix II) testing machines. Five specimens of each composition were tested with displacement rate of 0.75 mm/min.

#### Tensile Test

Tensile tests were performed using an MTS Exceed E42 universal testing machine with a 500N load cell to obtain the engineering stress–strain curve, the Young's modulus (determined from the initial linear elastic region of the stress–strain curve), the yield stress (the stress at the maximum), the elongation to break, and the toughness (as measured from the area under the stress–strain curve). Dogbone samples were cut or molded (for brittle specimens) with a 3.15 mm width, 0.1 mm thickness and the gage length was ≈15 mm. The specimens were clamped in the grip areas and tested under uniaxial tensile loading at a strain rate of 0.006 min<sup>-1</sup>.



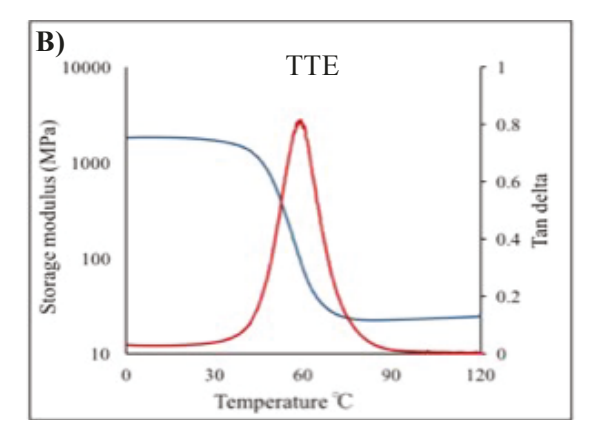


**Figure S1.** The tan  $\delta$  curves and storage modulus curves of control-based and TTE based composites, obtained from DMTA measurements at 1 Hz.

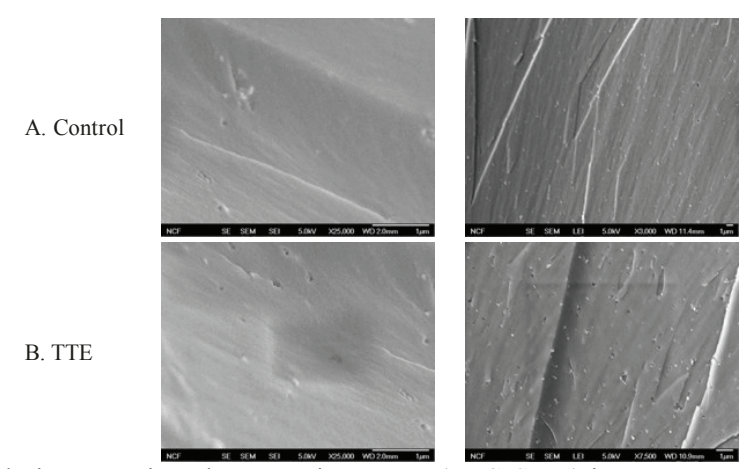


**Figure S2.** High-resolution scanning electron microscopy (FEG-SEM) images were taken for surfaces of A. control and B. TTE composites.

**Table S1.** Mechanical properties of both control TTE based composites obtained from tensile testing at  $0.0001 \text{ s}^{-1}$  displacement rate.

	Tensile strength (MPa)	Elongation at break (%)	Toughness (MJ/m³)
Control composite	$3 \pm 0.3$	$35 \pm 4$	$0.5 \pm 0.1$
TTE composite	6 ± 1	$55 \pm 10$	$1.9 \pm 0.4$

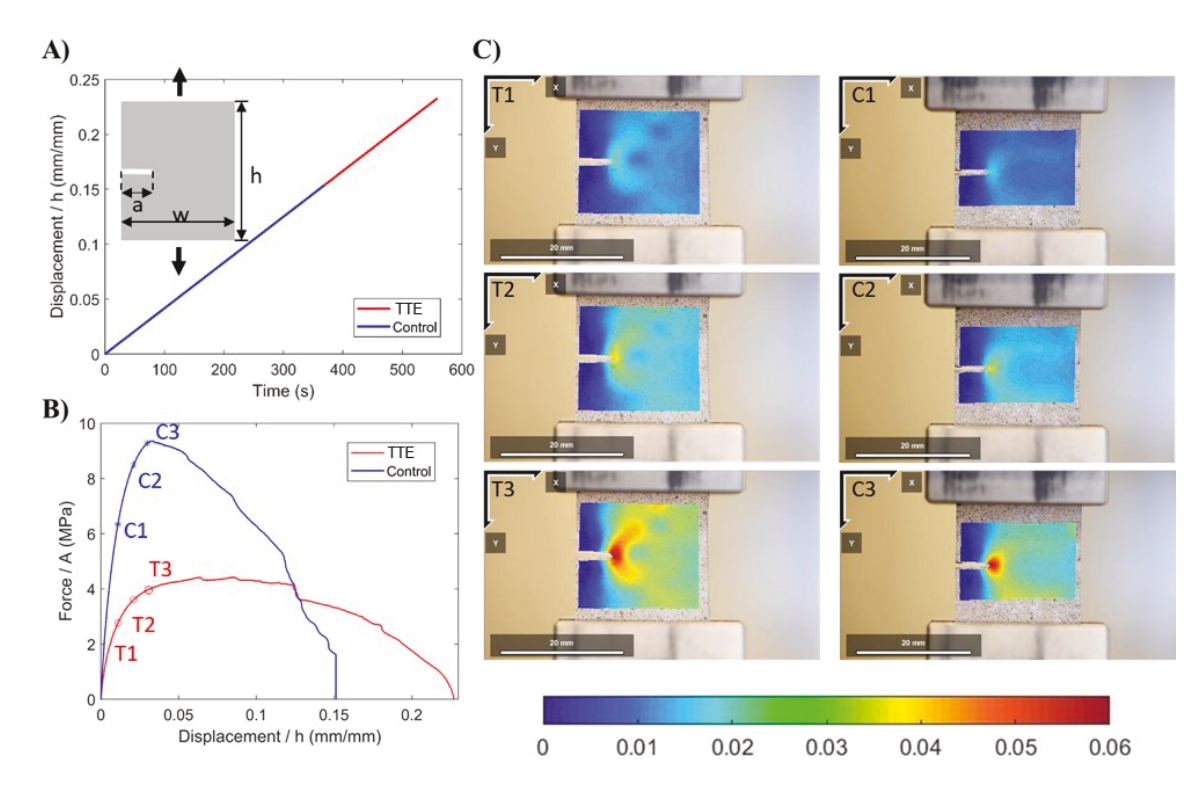


**Figure S3.** A) Loading history in terms of the global strain  $\Delta/h$  versus time and B) Nominal tensile stress (force / cross-section area) versus global strain of the single edge notch fracture test using another set of control and TTE-activated samples. C) Spatial distribution of the vertical normal strain components  $\varepsilon_{yy}$ , measured using DIC, at different time frames before crack propagation: T1/C1 (global strain = 1%); T2/C2 (global strain = 2%); T3/C3 (global strain = 3%). Similar to **Figure 3**, the TTE-activated sample also exhibited a more diffusive (i.e., less concentrated) crack tip strain field than the control sample.

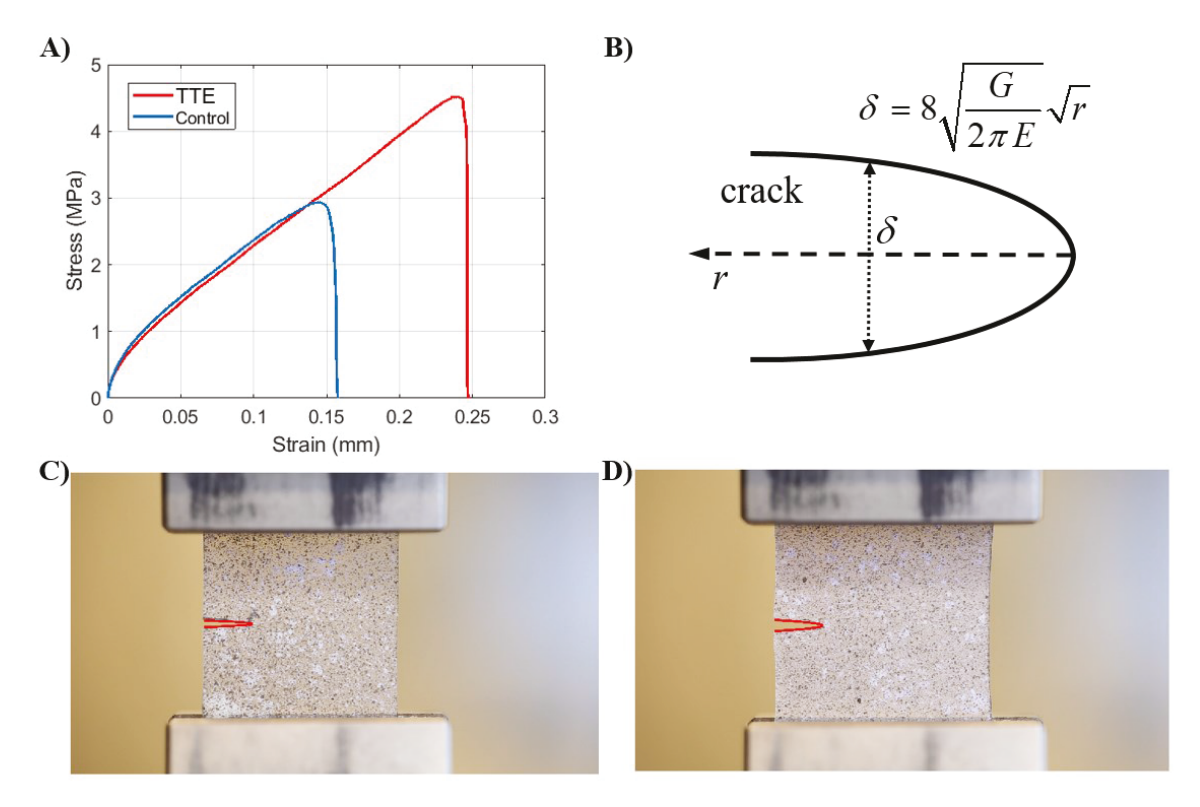


Figure S4. Evaluation of fracture energy  $G_c$  based on the crack opening profile. A) Engineering stress-strain curves under uniaxial tension for the control and TTE-activated composites used in the fracture tests as shown in Figure 3. The slope of the linear portion was taken as the Young's modulus E, which was 17.3MPa and 18.0MPa for the control and TTE-activated composites, respectively. B) Parabolic crack opening profile for a plane-stress Mode-I crack predicted by the fracture mechanics theory. Fitting of the crack opening profile at the onset of crack propagation for the C) control sample and D) TTE-activated sample. The red lines represent the parabolic fits according to the equation in B), which yielded that  $G_c = 260 \text{ J/m}^2$  and 550 J/m² for the control and TTE activated samples, respectively.

**Video S1.** Strain fields in notched TTE and control samples under tension mapped using Digital Image Correlation.

Video S2. Failure of the control 2 notch sample under 3-point bend test at 0.75 mm/min loading rate.

Video S3. Failure of the TTE 2 notch sample under 3-point bend test at 0.75 mm/min loading rate.

**Table S2**. Mechanical properties of 2-notches samples of both control and TTE based composite under 3-point bend test.

	Maximum stress (MPa)	Elongation at break (%)	Toughness (MJ/m <sup>3</sup> )
Control	$12 \pm 3$	$10 \pm 8$	$1.9 \pm 0.5$
TTE	$28 \pm 6$	$30 \pm 10$	$6.1 \pm 0.9$

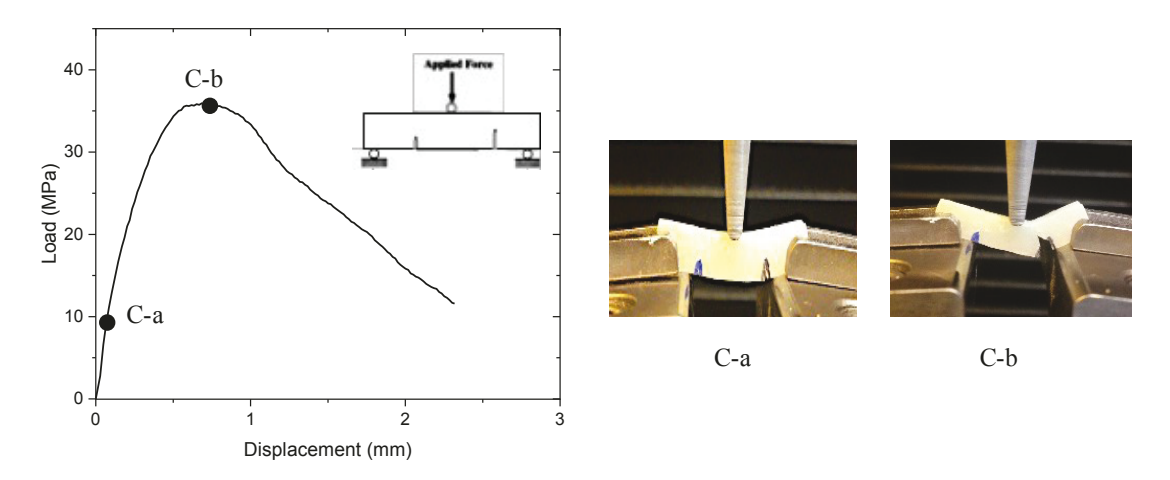


**Figure S5.** Load-displacement profiles from fracture of double-notched composite specimens and images of the two uneven notches before and after failure at a displacement rate 0.75 mm/min.

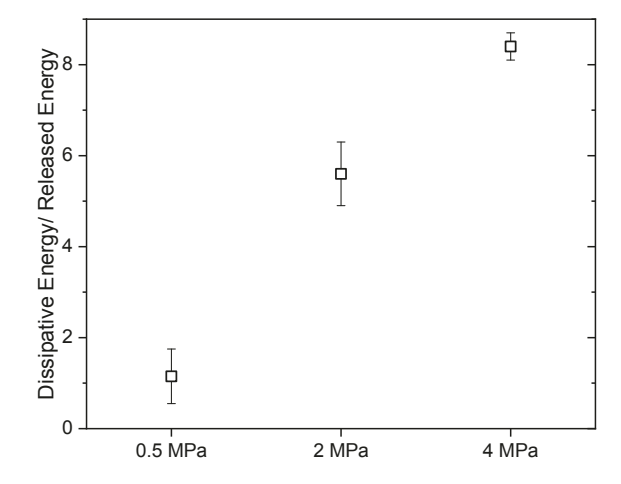


**Figure S6**. The ratio between the dissipative energy and the released energy of TTE based composites upon applying cyclic loading up to 3 stress level 0.5 MPa, 2 MPa and 4 MPa followed by release of the stress.

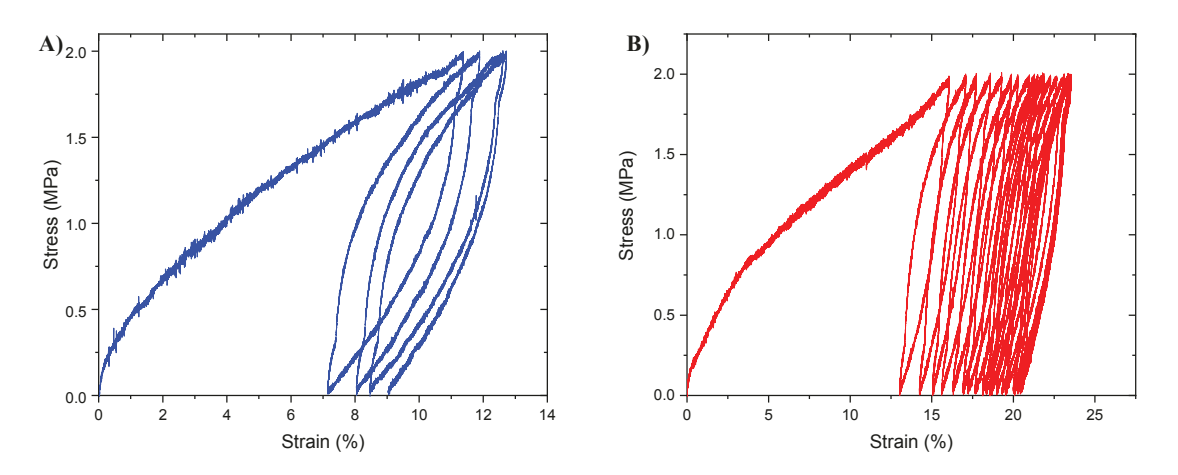


**Figure S7**. Hysteresis loop cycles during loading of 2 MPa stress then unloading to 0 MPa at 0.1 mm min<sup>-1</sup> rate for both control and TTE enabled composite.